

A Hierarchical Hybrid MXenes Interlayer with Triple Function for Room-Temperature Sodium-Sulfur Batteries

Zefu Huang, Shijian Wang, Xin Guo,* Javad Safaei, Yaojie Lei, Wei-Hong Lai, Xiuyun Zhang, Bing Sun,* Devaraj Shanmukaraj, Michel Armand, Teofilo Rojo, and Guoxiu Wang*

Room temperature sodium sulfur (RT Na-S) batteries with high theoretical energy density and low cost have recently gained extensive attention for potential large-scale energy storage applications. However, the shuttle effect of sodium polysulfides is still the main challenge that leads to poor cycling stability, which hinders the practical application of RT Na-S batteries. Herein, a multifunctional hybrid MXene interlayer is designed to stabilize the cycling performance of RT Na-S batteries. The hybrid MXene interlayer comprises a large-sized $Ti_3C_2T_x$ nanosheets inner layer followed by a small-sized $Mo_2Ti_2C_3T_x$ nanoflake outer layer on the surface of the glass fiber (GF) separator. The large-sized $Ti_3C_2T_x$ nanosheet inner layer provides an effective physical block and chemical confinement for the soluble polysulfides. The small-sized $Mo_2Ti_2C_3T_x$ outer layer offers an excellent polysulfide trapping capability and accelerates the reaction kinetics of polysulfide conversion, due to its superior electronic conductivity, large specific surface area, and Mo-rich catalytic surfaces. As a result, RT Na-S batteries with this hybrid MXene interlayer modified glass fiber separator deliver a stable cycling performance over 200 cycles at 1 C with an enhanced capacity retention of 71%. This unique structure design provides a novel strategy to develop 2D material-based functional interlayer for high-performance metal-sulfur batteries.

1. Introduction

RT Na-S batteries have attracted increasing interest due to their high theoretical energy density (1672 mAh g^{-1}),^[1] high energy efficiency of charge–discharge, excellent life cycle, and low cost of the electrode materials, which exhibit the potential to become promising alternatives to replace the state-of-the-art lithium-ion (Li-ion) batteries for future grid energy storage. However, the shuttle effect of soluble sodium polysulfides (Na_2S_8 , Na_2S_6 , and Na_2S_4) generated during discharge–charge leads to a loss of active material and unstable cycling performance, which is still challenging to the practical application of RT Na-S batteries.^[2–4]

Different strategies have been reported to alleviate the shuttling of soluble polysulfides in the RT Na-S battery system, including improving the cathode host design to form suitable porous structures for physically trapping the polysulfides,^[5–10] optimizing liquid electrolytes by using novel additives, applying

(quasi-)solid-state electrolytes to reduce the solubility of polysulfides,^[11–16] and modifying the separator to immobilize polysulfides at the cathode side.^[17–25] Among these methods,

Z. Huang, S. Wang, X. Guo, J. Safaei, B. Sun, G. Wang
Centre for Clean Energy Technology
School of Mathematical and Physical Sciences
Faculty of Science
University of Technology Sydney
Ultimo, NSW 2007, Australia
E-mail: xin.guo@uts.edu.au; bing.sun@uts.edu.au;
guoxiu.wang@uts.edu.au

Y. Lei, W.-H. Lai
Institute for Superconducting & Electronic Materials
University of Wollongong
Innovation Campus
Wollongong, NSW 2500, Australia
X. Zhang
College of Physical Science and Technology
Yangzhou University
Yangzhou 225002, China
D. Shanmukaraj, M. Armand
Centre for Cooperative Research on Alternative Energies (CIC
energiGUNE)
Basque Research and Technology Alliance (BRTA)
Alava Technology Park
Albert Einstein 48, 01510 Vitoria-Gasteiz, Spain
T. Rojo
Inorganic Chemistry Department
University of the Basque Country UPV/EHU
P.O. Box. 644, 48080 Bilbao, Spain

 The ORCID identification number(s) for the author(s) of this article can be found under <https://doi.org/10.1002/admt.202202147>

© 2023 The Authors. Advanced Materials Technologies published by Wiley-VCH GmbH. This is an open access article under the terms of the Creative Commons Attribution License, which permits use, distribution and reproduction in any medium, provided the original work is properly cited.

DOI: 10.1002/admt.202202147

introducing a functional interlayer between the separator and the sulfur cathode (also known as modified separators) is a facile and efficient strategy to suppress the shuttle effect, as it avoids a complicated fabrication process and maintains the energy density of sulfur cathodes. For example, sodiated-Nafion coated polypropylene (PP) separators have been employed to realize improved ion selectivity, which could permit Na^+ transfer but restrict polysulfide permeation.^[17–19] Later, a number of inorganic materials with strong chemical adsorption and high catalytic effects, such as Pt, Co, Ni, FeS_2 , MoS_2 , and MoSe_2 , have been investigated as functional interlayers to address the polysulfides shuttling concerns and improve the cycling performance.^[24,26–33]

Recently, 2D materials such as MXenes and thin layers of MOF particles have been used as the functional interlayer to modify separators, due to their large aspect ratio, excellent flexibility, and tunable interlayer spacing (allowing selective ion transport). In particular, MXenes, as a new class of 2D transition metal carbides and/or nitrides, have shown promising potential for alkali metal-chalcogenides batteries. Beyond the common advantages of 2D materials mentioned above, MXenes also show excellent metallic conductivity, strong chemical adsorption and catalytic conversion toward the polysulfides, thereby boosting the reaction kinetics and elevating the electrochemical performance of sulfur-based batteries.^[10,25,34–45] Currently, the MXene family is already very large, with various members containing redox-active transition metals such as V, Ta, Cr, Nb, and Mo.^[46] Among these elements, Mo bonds with C and N to form MoC or MoN dictated on the surface of MXenes have demonstrated catalytic roles to promote the conversion reactions from soluble long-chain polysulfides to short-chain solid discharge products, which fundamentally inhibit the shuttle effects of RT Na-S batteries.^[22–23,47] However, these still lacked a rationally designed interlayer that could maximize the functionalities of MXenes and enhance the electrochemical performance of RT Na-S batteries.

Herein, we designed a hierarchical hybrid MXene-based interlayer by integrating one layer of large-sized $\text{Ti}_3\text{C}_2\text{T}_x$ nanosheets with another layer of small-sized $\text{Mo}_2\text{Ti}_2\text{C}_3\text{T}_x$ nanoflakes to simultaneously exploit the physical and chemical functions of hybrid MXenes (Figure 1). The large-sized $\text{Ti}_3\text{C}_2\text{T}_x$ nanosheets layer directly coated onto the glass fiber separator offers much smaller channels that can effectively block the permeation of polysulfide molecules and prevent the puncture of small pieces of $\text{Mo}_2\text{Ti}_2\text{C}_3\text{T}_x$ to the macroporous glass fiber (GF) separator (which easily leads to a short circuit). The outer layer of small-sized $\text{Mo}_2\text{Ti}_2\text{C}_3\text{T}_x$ nanoflakes has more exposed active sites that can efficiently adsorb and accelerate the conversion of soluble long-chain Na polysulfides into solid short-chain Na polysulfides, and thus keeps the active materials on the cathode side of the system and contributes to a high reversible capacity and stable cycling performance. This work provides a new strategy to improve the functioning of separators in RT Na-S batteries by optimizing the interlayer structure and adding catalytic components.

2. Results and Discussion

The hybrid MXene interlayer consists of two different layers of MXenes, which were prepared through wet-etching methods.^[46,48–50] The large-sized $\text{Ti}_3\text{C}_2\text{T}_x$ nanosheets were selected to construct the inner layer directly attached to the GF sep-

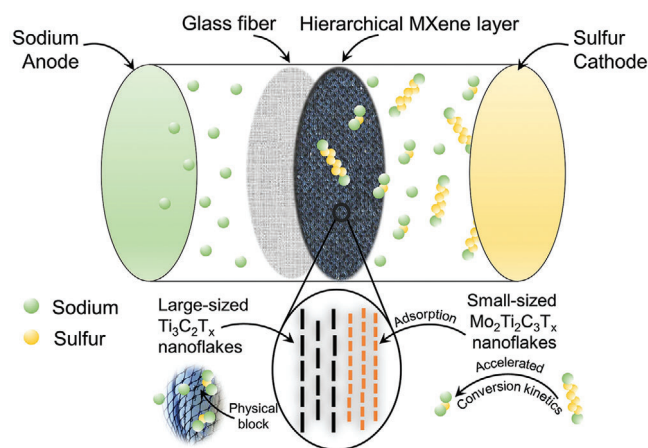


Figure 1. Schematic of the configuration of the room temperature sodium sulfur (RT Na-S) battery system with the hierarchical MXene interlayer on the glass fiber separator.

arator, and the small-sized $\text{Mo}_2\text{Ti}_2\text{C}_3\text{T}_x$ nanoflakes were used to fabricate the outer layer that faces the sulfur cathodes, as shown in Figure 1. To prepare the large-sized $\text{Ti}_3\text{C}_2\text{T}_x$ nanosheets, a mild etchant of LiF and HCl rather than the concentrated HF was employed to treat the Ti_3AlC_2 MAX precursor (see details in Supporting Information). The reacted sediment was washed with de-ionized water and sonicated to obtain the delaminated $\text{Ti}_3\text{C}_2\text{T}_x$ nanosheets. The vanishing of the characteristic peaks of Ti_3AlC_2 and the shift of the (002) peak to a lower angle in the XRD result of the derived sample demonstrates the successful exfoliation and delamination of the $\text{Ti}_3\text{C}_2\text{T}_x$ (Figure S1, Supporting Information). After that, the suspension was centrifuged at 6000 rpm to select the large-sized $\text{Ti}_3\text{C}_2\text{T}_x$ nanosheets in the sediment. The topography of the $\text{Ti}_3\text{C}_2\text{T}_x$ MXene is measured by AFM and exhibits typical nanosheet morphology with a lateral size ranging from 2.5 to 3.8 μm (Figure S2, Supporting Information).

Subsequently, the small-sized $\text{Mo}_2\text{Ti}_2\text{C}_3\text{T}_x$ nanoflakes were prepared by etching the $\text{Mo}_2\text{Ti}_2\text{AlC}_3$ MAX with a concentrated HF solution (48%) at 55 $^\circ\text{C}$ for 120 h. The resultant mixture was thoroughly washed with deaerated water until the pH value reached 6. The obtained sediment was then treated with TBAOH to achieve TBA^+ intercalated MXene, which was further delaminated under ultrasonication. Finally, the suspension was centrifuged at 3500 rpm for 25 min to separate few-layer $\text{Mo}_2\text{Ti}_2\text{C}_3\text{T}_x$ nanoflakes (supernatant) from the unreacted MAX and multilayer MXene (sediment). The comparison of the XRD patterns presents an obvious (002) peak shift from 14.9 $^\circ$ in the raw $\text{Mo}_2\text{Ti}_2\text{AlC}_3$ material to 5.6 $^\circ$ in the as-prepared $\text{Mo}_2\text{Ti}_2\text{C}_3\text{T}_x$ (Figure 2a), indicating the remarkable increase of interlayer spacing from MAX phase to 2D MXene. Besides this effect, the crystalline peaks of $\text{Mo}_2\text{Ti}_2\text{AlC}_3$ completely disappeared in the derived $\text{Mo}_2\text{Ti}_2\text{C}_3\text{T}_x$, demonstrating the success of the exfoliation and delamination processes.

The morphology and microstructure of the $\text{Mo}_2\text{Ti}_2\text{C}_3\text{T}_x$ nanoflakes were characterized by SEM and TEM techniques. The SEM image of the etched sample shows an accordion-like morphology, which implies the extraction of Al layer from the MAX precursor (Figure 2b). The delaminated $\text{Mo}_2\text{Ti}_2\text{C}_3\text{T}_x$ presents a typical 2D nanosheet morphology with the average size of around

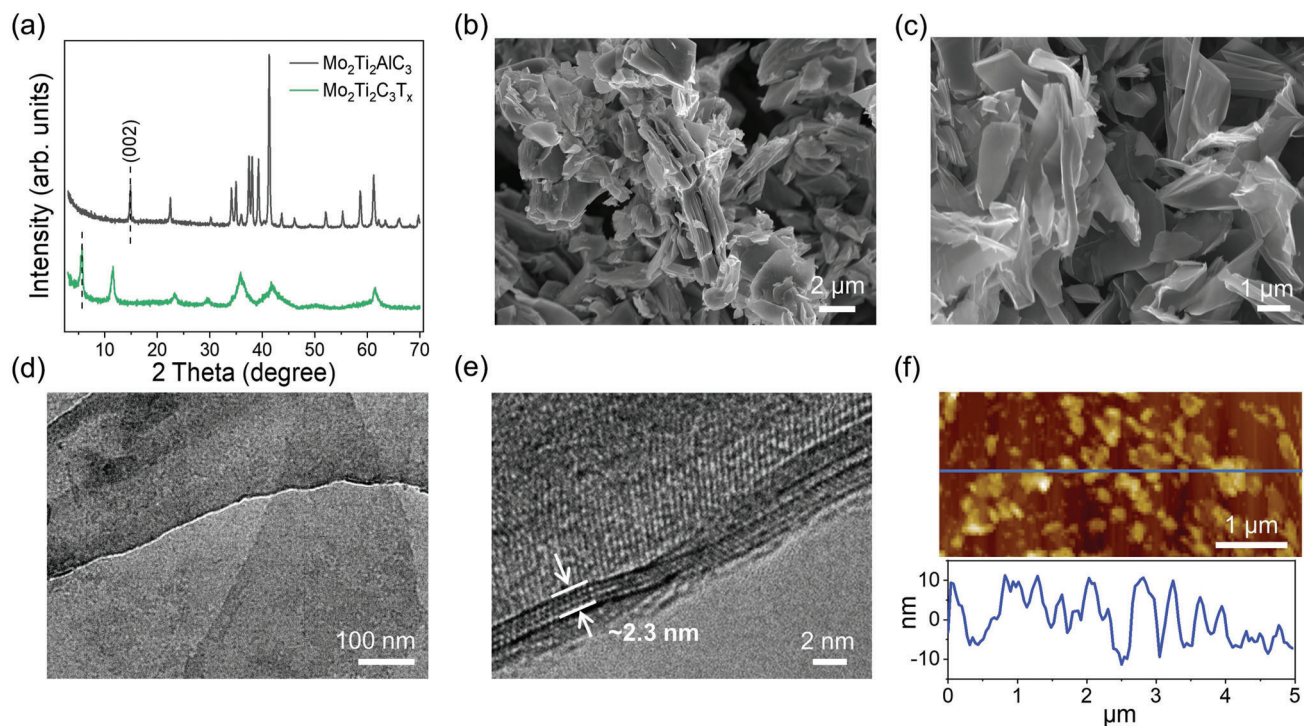


Figure 2. a) XRD pattern comparison between $\text{Mo}_2\text{Ti}_2\text{AlC}_3$ and $\text{Mo}_2\text{Ti}_2\text{C}_3\text{T}_x$. Scanning electron microscopy (SEM) images of b) etched $\text{Mo}_2\text{Ti}_2\text{AlC}_3$ and c) delaminated few-layer $\text{Mo}_2\text{Ti}_2\text{C}_3\text{T}_x$. d) Low-magnification and e) high-magnification transmission electron microscopy (TEM) image of few-layer $\text{Mo}_2\text{Ti}_2\text{C}_3\text{T}_x$. f) Atomic force microscopy (AFM) topography of $\text{Mo}_2\text{Ti}_2\text{C}_3\text{T}_x$ flakes and the corresponding height profile along the marked blue line.

400 to 500 nm (Figure 2c,d). The TEM image with high resolution in Figure 2e shows a monolayer $\text{Mo}_2\text{Ti}_2\text{C}_3\text{T}_x$ consisting of four metal atomic layers with a thickness of 2.3 nm. Compared with its piece size shown in Figure 2c,d, the delaminated $\text{Mo}_2\text{Ti}_2\text{C}_3\text{T}_x$ nanoflakes provide a very large aspect ratio of approximately 500:2, which is beneficial to adsorb and accelerate the conversion of polysulfides. The topography profile of $\text{Mo}_2\text{Ti}_2\text{C}_3\text{T}_x$ also indicates its lateral size is around 0.5 μm on average (Figure 2f). The much smaller size of $\text{Mo}_2\text{Ti}_2\text{C}_3\text{T}_x$ flakes can be attributed to the harsh etching environment, long etching time, and extensive mechanical shearing during the preparation process.

XPS was used to understand the surface chemistries of the as-prepared $\text{Mo}_2\text{Ti}_2\text{C}_3\text{T}_x$ nanoflakes (Figure S3, Supporting Information). The predominant peaks at 228.9 and 232.1 eV in the Mo 3d XPS spectrum can be assigned to C–Mo– T_x bonds, which is in accordance with the atomic structure in the theoretical study.^[51] The small peaks at the binding energy of 230.3 (233.5) and 232.6 (235.6) eV (numbers in parenthesis represent the peak of Mo 3d_{3/2}) can be assigned to the Mo^{+5} 3d_{5/2(3/2)}} and Mo^{+6} 3d_{5/2(3/2)}}, respectively, originating from the inevitable surface oxidation of the $\text{Mo}_2\text{Ti}_2\text{C}_3\text{T}_x$.^[52] The C–Ti and C–Mo/Ti– T_x bonds located at 282.1 and 282.6 eV in the C 1s region further confirm the local environment of Ti and Mo metal elements.^[51,53,54] All these measurements comprehensively confirm that few-layer $\text{Mo}_2\text{Ti}_2\text{C}_3\text{T}_x$ nanoflakes with a smaller lateral size have been prepared successfully.

Small-sized $\text{Mo}_2\text{Ti}_2\text{C}_3\text{T}_x$ nanoflakes were selected to prepare the outer layer of the hybrid MXene interlayer because of the ideally exposed catalytic Mo atom layer (Figures 3a,b) and its rela-

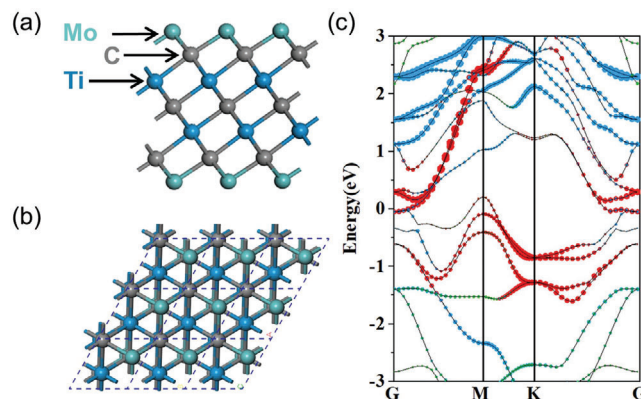


Figure 3. Schematic of the a) side view and b) top view of the $\text{Mo}_2\text{Ti}_2\text{C}_3\text{T}_x$ structure. c) Band structure and density of states (DOS) of $\text{Mo}_2\text{Ti}_2\text{C}_3\text{T}_x$.

tively good stability. To the best of our knowledge, it is the first time $\text{Mo}_2\text{Ti}_2\text{C}_3\text{T}_x$ was applied in RT Na-S batteries. Density functional theory (DFT) calculation was further applied to investigate the electronic structure of $\text{Mo}_2\text{Ti}_2\text{C}_3$ MXene. The band structure and density of states (DOS) in Figure 3c indicate that the $\text{Mo}_2\text{Ti}_2\text{C}_3$ monolayer is metallic, which is similar to the Ti_3C_2 MXene.^[55–57] The high electronic conductivity of this coating layer could reduce the internal impedance and benefit fast reaction kinetics for polysulfide conversion in RT Na-S batteries.

To prepare the hybrid MXene interlayer, the as-prepared $\text{Ti}_3\text{C}_2\text{T}_x$ and $\text{Mo}_2\text{Ti}_2\text{C}_3\text{T}_x$ colloidal solutions were mixed with

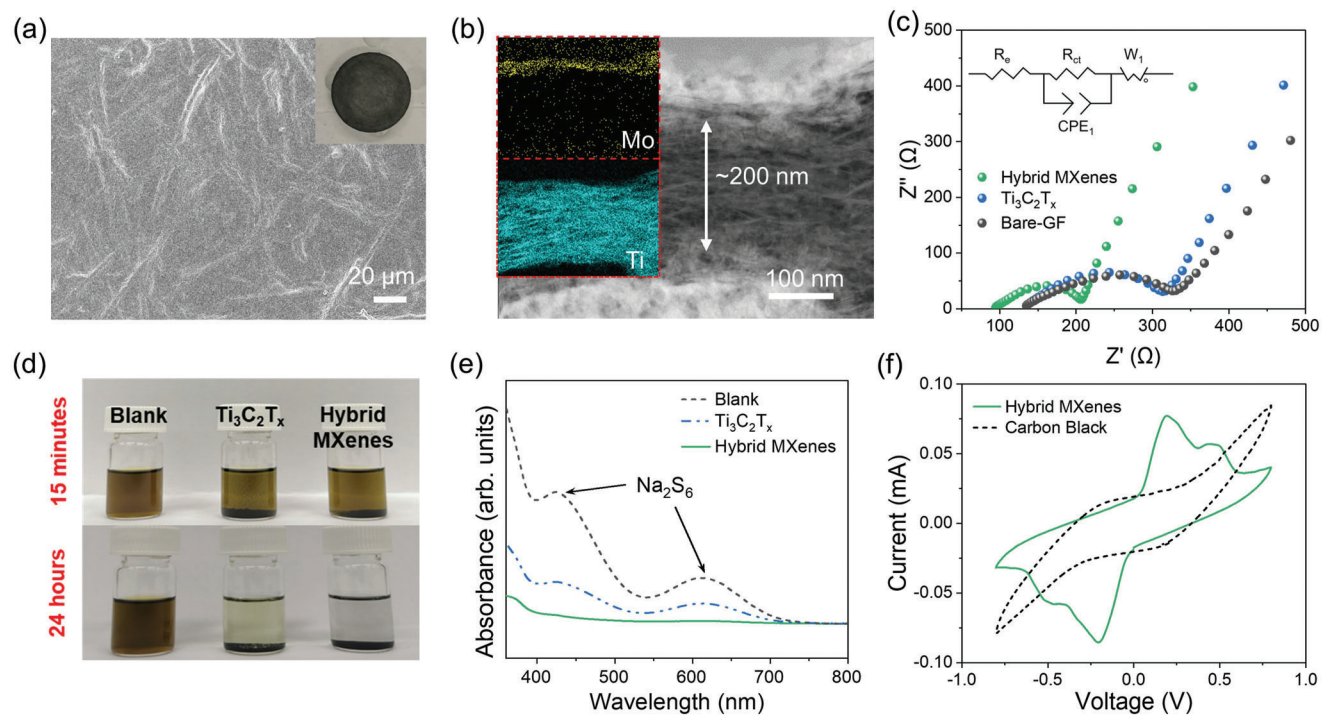


Figure 4. a) SEM image of the surface of a GF@Hybrid MXene separator; Inset is a digital photo of the separator. b) Cross-sectional scanning transmission electron microscope (STEM) image of a GF@Hybrid MXene separator; inset is the EDS mapping results of Mo and Ti elements. c) Electrochemical impedance spectroscopy (EIS) spectra of the Na-S cells using GF@Hybrid MXene, GF@Ti₃C₂T_x, and bare GF as separators, respectively (Inset is the equivalent circuit). d) Digital photos of the blank Na₂S₆ solution and the solution with Ti₃C₂T_x, and hybrid MXenes after 15 min and 24 h. e) UV-Vis spectra of the blank Na₂S₆ solution and the solution with Ti₃C₂T_x, and hybrid MXenes after 24 h. f) Cyclic voltammogram (CV) curves of hybrid MXene | Na₂S₆ | hybrid MXene and carbon black | Na₂S₆ | carbon black symmetric cells at a scan rate of 0.1 mV s⁻¹.

PTFE in a mass ratio of 95: 5 and then dispersed in isopropanol by ultrasonication, respectively. Here the PTFE works as a binder to bridge the MXenes and GF separator. The large-sized Ti₃C₂T_x nanosheet inner layer was deposited on the surface of the GF separator by directly dropping the suspension on the separator. Then, the small-sized Mo₂Ti₂C₃T_x outer layer was deposited on top of the Ti₃C₂T_x layer via the same method to form a complete hybrid MXene interlayer coated GF (GF@Hybrid MXene) separator. Meanwhile, a solely Ti₃C₂T_x coated separator (GF@Ti₃C₂T_x) with the same total loading amount of MXenes was also prepared for comparison. For the hybrid MXene interlayer, large-sized Ti₃C₂T_x nanosheets can directly provide a physical block to the sodium polysulfides, and in the meantime, they can improve the kinetics of the transition of polysulfides.^[20,39] Meanwhile, the small-sized Mo₂Ti₂C₃T_x nanoflakes coated on the large-sized Ti₃C₂T_x layers have the excellent binding capability with the sodium polysulfides, which are blocked by the Ti₃C₂T_x nanosheets and thus confine and accelerate the transformation of soluble polysulfides on the cathode side.^[58] To learn the possible interaction between the Ti₃C₂T_x layer and Mo₂Ti₂C₃T_x layer, the zeta potential testing was used to study the surface charge of both Ti₃C₂T_x and Mo₂Ti₂C₃T_x in an aqueous solution with the concentration of 0.01 mg mL⁻¹. According to the zeta potential measurement results (Figure S4, Supporting Information), both Ti₃C₂T_x and Mo₂Ti₂C₃T_x flakes have negative surface charges and no interaction appeared. Furthermore, Raman spectra measurements were applied to further confirm

the interaction between these two MXenes. The comparison among the intersection layer of hybrid MXene, Ti₃C₂T_x layer, and Mo₂Ti₂C₃T_x layer Raman spectra results (Figure S5, Supporting Information) shows that the peaks in the intersection layer of hybrid MXene are only coming from the superposition of the Ti₃C₂T_x layer peaks (199, 280, 375, 622, and 720 cm⁻¹)^[59-61] and the Mo₂Ti₂C₃T_x layer peaks (219, 383, 429, 645, and 732 cm⁻¹),^[62] indicating the excellent phase stability of the hybrid MXene. **Figure 4a** shows the SEM image and digital photo of the GF@Hybrid MXene separator. The macropores in GF (Figure S6, Supporting Information) have been covered by 2D MXenes in the GF@Hybrid MXene separator. The cross-sectional STEM image reveals that the hybrid MXene interlayer with an ultra-thin thickness of approximately 200 nm was successfully deposited on the separator surface (Figure 4b, and Figure S7, Supporting Information). The MXene layers with Mo element homogeneously deposited on the top of the MXene layers only containing Ti element (Figure 4b, insets) indicate the successful fabrication of the as-prepared hierarchical layered structure. The impedance of the as-prepared separators was evaluated in full Na-S cells by EIS. Figure 4c displays the Nyquist plots of the cells with different separators, in which the GF@Hybrid MXenes separator exhibits the lowest charge transfer resistance (206 Ω) in comparison with the GF@Ti₃C₂T_x (313 Ω) and bare-GF (326 Ω). The improved charge transfer kinetics can be ascribed to the balance of the electronic conductivity and ionic conductivity of GF@Hybrid MXenes deriving from the unique hierarchical structural design.

By contrast, the GF@Ti₃C₂T_x with stacked large flakes only shows sacrificed considerable electrolyte permeation capability.

The chemical adsorption and catalytic potential of the selected MXenes were measured before any battery testing. As shown in Figure 4d, the color of Na₂S₆ solution with hybrid MXenes (Ti₃C₂T_x and Mo₂Ti₂C₃T_x) changes from deep yellow to almost transparent after 24 h, while the solution with Ti₃C₂T_x has a color change from deep yellow to light green during the same time span, indicating the stronger adsorption capability of the hybrid MXene compared to the Ti₃C₂T_x. The results were further verified by the UV–Vis testing of the hybrid MXene and Ti₃C₂T_x soaked solution after 24 h (Figure 4e). The signals of Na₂S₆ weakened after treating with Ti₃C₂T_x, but almost vanished after mixing with hybrid MXenes in the same period. The excellent adsorption ability of hybrid MXenes can be ascribed to the more exposed active sites of the small-sized Mo₂Ti₂C₃T_x nanoflakes.

To investigate the catalytic function of hybrid MXenes for sodium polysulfide conversion, cyclic voltammetry (CV) curves of symmetric cells were gathered in a solution of 0.1 M Na₂S₆ in DEGDMC at a scan rate of 0.1 mV s⁻¹ (Figure 4f). The symmetric cells with carbon black loaded carbon cloth as cathodes show low current responses and no significant voltage peaks. In contrast, the symmetric cells with hybrid MXene loaded carbon cloth cathodes offer significantly higher current responses and two pairs of well-defined peaks (at -0.21/0.21 and -0.48/0.48 V, respectively). Because Na₂S₆ is the only active reactant in the symmetric cells, the peaks at -0.21 V almost certainly originated from the conversion of Na₂S₆ to Na₂S₂, and the peak at -0.48 V is ascribed to the reduction from Na₂S₂ to Na₂S. The redox peaks are still distinct, and a higher current response was observed when the scan rate increases to 0.5 mV s⁻¹ (Figure S8, Supporting Information), which implies the efficacy of hybrid MXenes' catalytic effects under different charging–discharging rates. These results validate that the hybrid MXenes can accelerate the conversion of sodium polysulfides.

The merits of GF@Hybrid MXene separator were examined in RT Na-S batteries by using porous carbon/sulfur composite (pC@S) as the cathode, 1 M NaClO₄ in EC/PC (1: 1 in vol) with 5% FEC as the electrolyte, and sodium metal disc as the anode. The porous carbon (pC) host was obtained by sintering the activated *Sterculia lychmophora* in Ar atmosphere in accordance with our precious work (Figures S9 and S10, Supporting Information). The sulfur loading in the pC@S was confirmed by XRD characterization, and the thermal gravimetric analysis result indicates the S content in the pC@S composite is around 53.5 wt% (Figure S11, Supporting Information). CV profiles of the RT Na-S battery with GF@Hybrid MXene separator were collected to understand the electrochemical behavior of the sulfur cathode during the charge–discharge processes. As shown in Figure 5a, two cathodic peaks at around 2.0 and 0.8 V appear in the first cycle. The peak at 2.0 V corresponds to the conversion from S₈ to long-chain Na₂S_x (4 < x ≤ 8) and irreversible side reactions between the carbonate-based electrolyte and the polysulfides.^[63] The peak at 0.8 V can be ascribed to the long-chain sodium polysulfides to short-chain solid-state Na₂S/Na₂S₂ conversion and the solid state interphase (SEI) formation.^[64] The broad anodic peak at around 1.9 V can be ascribed to the conversion reaction from insoluble Na₂S/Na₂S₂ to long-chain sodium polysulfides. In the second cathodic scan, the two prominent peaks convert to three new

peaks at 1.6, 1.2, and 0.84 V, corresponding to the conversion to Na₂S_x (4 < x ≤ 8), Na₂S₂ and Na₂S. The CV curves nearly overlap from the second cycle onwards, indicating the highly reversible electrochemical conversion reaction when using GF@Hybrid MXene separators. It is worth noting that the peak representing the formation of soluble long-chain Na₂S_x (4 < x ≤ 8) dramatically fades after the second cycle, which implies that S is quickly converted to insoluble short-chain sodium polysulfides with a very short existence of soluble long-chain sodium polysulfides due to the excellent catalytic effects of hybrid MXene interlayer.^[5,65]

Figure 5b shows the first and the second discharge–charge curves of an RT Na-S battery with GF@Hybrid MXene separator. The initial reversible capacity is 1016 mAh g⁻¹ with a Coulombic efficiency of 62%. The capacity fade in the first cycle could be assigned to the SEI layer formation and irreversible side reactions. In contrast, the RT Na-S battery with bare-GF separator provided a charge capacity of 697 mAh g⁻¹ with a low Coulombic efficiency of 43.3% (Figure S12, Supporting Information). The cycling performances of the RT Na-S cells at 0.1 C (1672 mA g⁻¹ = 1 C) with various separators (bare-GF, GF@Ti₃C₂T_x, and GF@Hybrid MXenes) are shown in Figure 5c. The GF@Hybrid MXene offered the highest capacity of 992 mAh g⁻¹ in discharge from the second cycle and retained a capacity of 620 mAh g⁻¹ after 100 cycles with the smallest capacity degradation of 0.36% per cycle. By contrast, the batteries with bare-GF and GF@Ti₃C₂T_x separators can only provide a respective capacity of 240 and 387 mAh g⁻¹ after 100 cycles.

Figure 5d exhibits the rate performance of the RT Na-S batteries with various separators. The cell with GF@Hybrid MXene separator achieved a reversible capacity of 316 mAh g⁻¹ at a high current of 2 C, and the capacity recovered to 860 mAh g⁻¹ when the current density was decreased to 0.5 C. In contrast, the cells with bare-GF and GF@Ti₃C₂T_x separators only exhibited low capacities of 52 and 112 mAh g⁻¹ at 2C, respectively. The enhanced cycling stability and rate performance of the batteries with the GF@Hybrid MXene separators can be attributed to the improved Na⁺ transport kinetics, good wettability in the carbonate-based electrolyte, and efficient interlayer structural design that can effectively trap the soluble polysulfides and accelerate the conversion kinetics. Consequently, the battery with GF@Hybrid MXene separator delivered a stable long-term cycling performance at a high current density (Figure 5e). After five activation cycles at 0.1 C, the cells achieved a reversible capacity of 562 mAh g⁻¹ at 1 C and remained around 357 mAh g⁻¹ after 500 cycles with a high average Coulombic efficiency of ≈99.5%. Notably, the Coulombic efficiencies in some cycles are slightly higher than 100% due to the oxidation of Na₂S to polysulfides in hybrid MXene interlayer and the recapture of those polysulfides by the cathode, which results in an extra charge capacity.^[14] Additionally, the RT Na-S batteries with GF@hybrid MXene separator also achieve a decent capacity of 531 mAh g⁻¹ at 1 C and a capacity retention of 302 mAh g⁻¹ after 100 cycles at a high sulfur loading of ≈2.2 mg cm⁻² (Figure S13, Supporting Information). Compared with previous works by applying MXene architectures in the RT Na-S battery system, this work indicates a new effective structural design and explores the function of Mo₂Ti₂C₃T_x applied in the RT Na-S batteries. Moreover, the hybrid MXene prepared in this work used a cheap and scalable method and achieved competitive electrochemical performance (Table S1, supporting information).

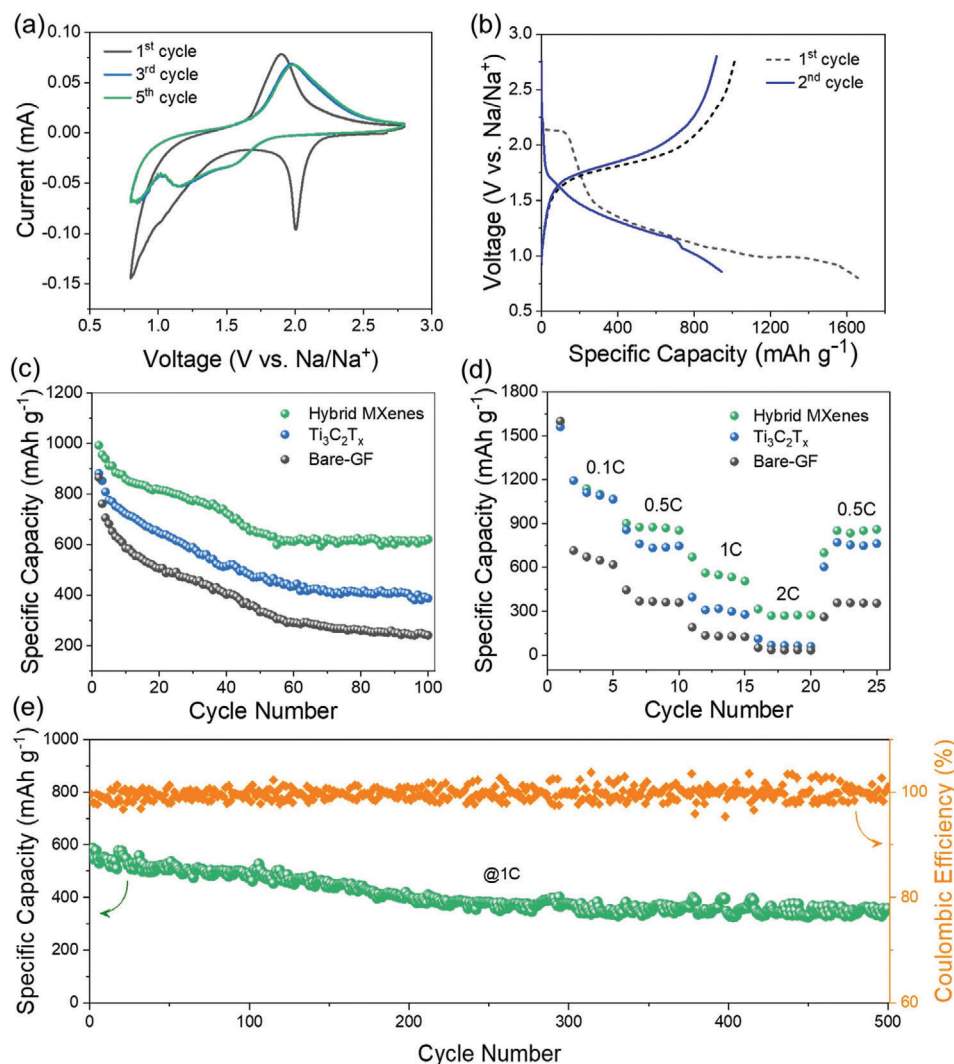


Figure 5. a) Selected CV profiles of the room temperature sodium sulfur (RT Na-S) battery with GF@Hybrid MXene separator at a scan rate of 0.1 mV s^{-1} . b) First and second discharge–charge curves of an RT Na-S battery with GF@Hybrid MXene separator. c) Cycling performance and d) rate performance of an RT Na-S battery with bare-GF, GF@ $\text{Ti}_3\text{C}_2\text{T}_x$, and GF@Hybrid MXene separators. e) Long-term cycling performance of the RT Na-S battery with GF@Hybrid MXene separator at 1 C rate.

To better verify and understand the mechanism and functions of the hybrid MXene interlayer, we performed in situ synchrotron XRD testing for the RT Na-S battery with GF@Hybrid MXene separator, as well as the postmortem characterizations on the separators and Na metal anodes from cycled RT Na-S batteries. As illustrated in **Figure 6a**, the S_8 (JCPDS no. 00-001-0478) and long-chain polysulfides (Na_2S_x , $6 \leq x \leq 8$) are both existing during the initial discharging from 2.4 to 1.5 V, and the S_8 transferred to long-chain polysulfides and Na_2S_4 (JCPDS no.00-071-0516) after discharging to 1.5 V.^[19] During the continuing discharge to 1.2 V, the Na_2S_4 further splits into short-chain sodium polysulfide Na_2S (JCPDS no. 04-003-6920).^[66,67] Subsequently, as shown in the following charge, the Na_2S_4 peak becomes weaker, which indicates the acceleration of the conversion from Na_2S transferring back to Na_2S_x ($6 \leq x \leq 8$) due to the MXene interlayer and thus reduces the shuttle effect and maintains a high reversible transition between short-chain polysulfides to long-chain polysulfides (Figure

S14, Supporting Information). In addition, there is no peak of Na_2S_2 detected during the discharge or charge, which might be due to the fast kinetically transition from Na_2S_4 to Na_2S .^[68]

For the postmortem characterizations, Figure S15 (Supporting Information) shows optical images of the GF@Hybrid MXene and bare-GF separators after 100 cycles. It can be seen that the hybrid MXene interlayers still maintain their integrity after cycling, and the anode side of the GF@Hybrid MXene separators displays a much lighter yellow color than those of the bare-GF separators. The yellow color can be assigned to the accumulation of insoluble sodium sulfides on the anode surface, from the reaction between the shuttled soluble long-chain sodium polysulfides and Na metal anode, leading to the active material loss in the battery. Moreover, some dark areas were observed on the anode side of bare-GF separator, which could be the consequence of the formation of sodium dendrites and continuous side reactions with shuttled polysulfides.^[69–72] Fewer dark spots were

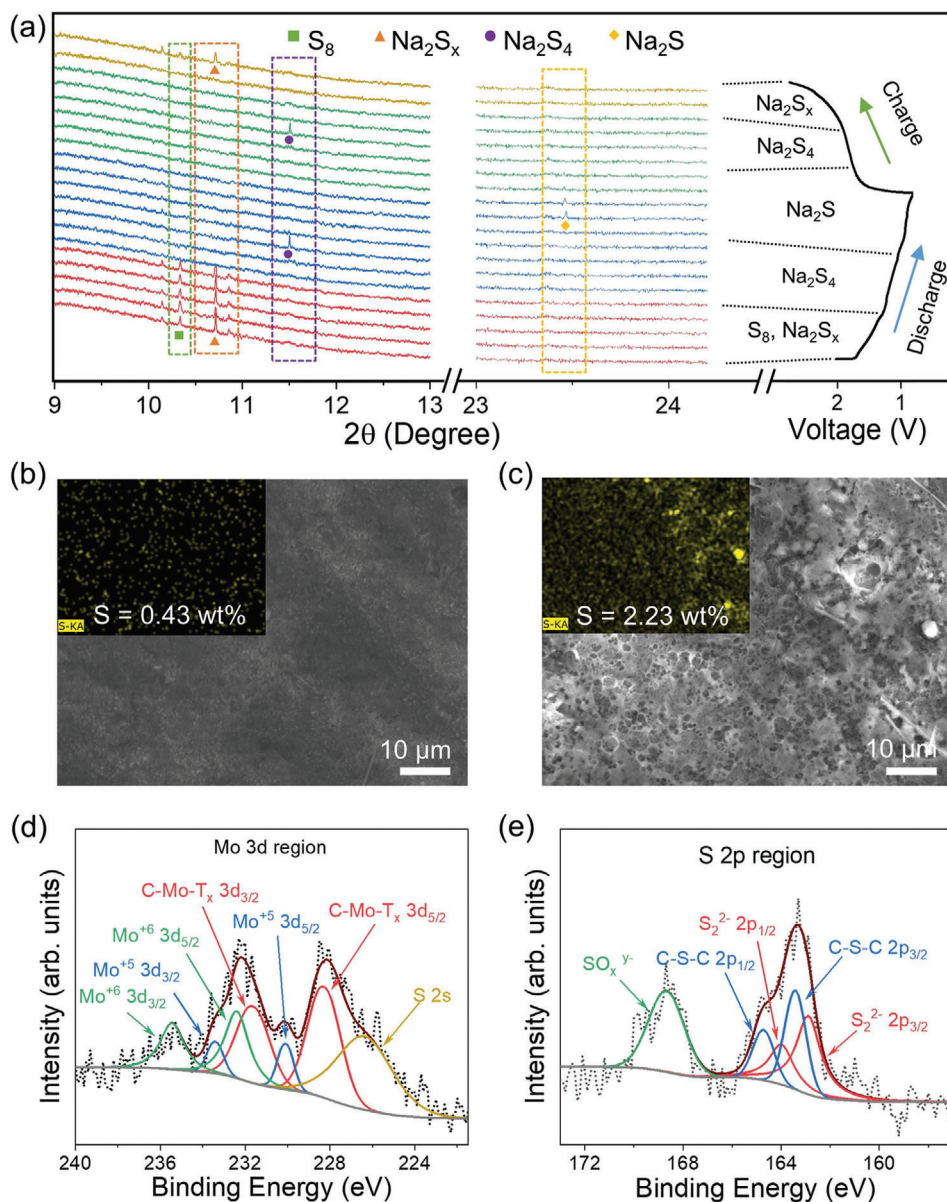


Figure 6. a) In situ synchrotron XRD pattern of the RT Na-S cell with GF@Hybrid MXene separator and the corresponding discharge–charge curves at 0.1 C. The scanning electron microscopy (SEM) images of sodium metal anode surface of RT Na-S batteries after 100 cycles using b) GF@Hybrid MXene and c) bare-GF separators, respectively; insets are the corresponding sulfur elemental mapping results. The XPS analysis of the cycled GF@Hybrid MXene separator in the d) Mo 3d region and e) S 2p region.

visualized in the modified separator, indicating that the GF@hybrid MXene can suppress the dendrite formation to some extent. To further verify the function of GF@Hybrid MXene separator to the cycling performance of Na metal anode, the Na|GF@Hybrid MXene|Na and Na|GF|Na symmetric cells were assembled and tested at the current of 1 mA cm^{-2} with the capacity limitation of 1 mAh cm^{-2} (Figure S16, Supporting Information). The Na|GF|Na cell occurred short circuit after around 257 h of cycling, while the Na|GF@Hybrid MXene|Na cells can keep stable cycling after 300 h, which indicates the hybrid MXene interlayer can regulate sodium plating/stripping and suppress Na dendrite formation.

Moreover, the sodium metal anodes of the cells with GF@Hybrid MXene separator and bare-GF separator were investigated by using the SEM and EDS mapping techniques. As exhibited in Figures 6b,c, the cycled Na metal anode from a cell with a GF@Hybrid MXene separator displays a much smoother surface than that from the bare-GF separator anode, which indicates that the hybrid MXene interlayer could deliver effective protection to the Na metal anode by providing a more homogeneous Na plating/stripping during cycling due to its active interaction with Na^+ flux. Moreover, the content of sulfur on the surface of Na metal anode from the cell with GF@Hybrid MXene separator is 0.43 wt%, which is significantly lower than that from

the cell with bare-GF separator (2.23 wt%), demonstrating the effectiveness of the hierarchically structured hybrid MXene interlayers for polysulfides immobilization. The cathode side surface of GF@Hybrid MXene separator after cycling was studied by using XPS. In the Mo 3d spectrum (Figure 6d), the emergent peak at 226.4 eV can be ascribed to Mo-S bond, which verifies the chemical interactions between $\text{Mo}_2\text{Ti}_2\text{C}_3\text{T}_x$ and sodium polysulfides.^[73–75] The S_{2-} signal located at 162.8 and 163.9 eV in the S 2p spectrum further confirms the existence of Mo-S bonds (Figure 6e).^[74,75]

Overall, the as-designed hierarchical hybrid MXene-modified separators improve the electrochemical performance of RT Na-S batteries from the following four aspects. Firstly, the hierarchical architecture of the hybrid MXene interlayer with large-sized $\text{Ti}_3\text{C}_2\text{T}_x$ nanosheets as the inner layer efficiently blocks the soluble sodium polysulfides passing through the separator. Secondly, owing to the polar surface of $\text{Ti}_3\text{C}_2\text{T}_x$ and $\text{Mo}_2\text{Ti}_2\text{C}_3\text{T}_x$, the hybrid MXenes display strong chemical adsorption capabilities for the long-chain polysulfides. Thirdly, the $\text{Mo}_2\text{Ti}_2\text{C}_3\text{T}_x$ with superior conductivity and catalytic activity can re-utilize and facilitate the conversion of retained sodium polysulfides and contribute to high capacity and long-term cycling performance. Fourthly, the hierarchical MXene interlayer regulates the Na^+ flux and benefits uniform sodium plating/stripping at anodes. All these factors synergistically lead to the significantly improved rate performance and cycling stability of these RT Na-S batteries.

3. Conclusion

In conclusion, a novel hierarchical structured hybrid MXene interlayer was prepared by sequentially coating the larger size-scale $\text{Ti}_3\text{C}_2\text{T}_x$ followed by smaller size-scale $\text{Mo}_2\text{Ti}_2\text{C}_3\text{T}_x$ onto glass fiber separators. The resultant multifunctional hybrid MXene-modified separator efficiently immobilizes polysulfides at the cathode side via the synergistic effects of physical blocking, chemical adsorption, and promotion of the conversion from sodium polysulfides to insoluble sodium sulfides. Meanwhile, the hybrid MXene interlayer protects sodium anodes by providing homogeneous Na^+ ion diffusion and suppressing the deposition of the sulfur species on the anode surface. As a result, the RT Na-S batteries with GF@Hybrid MXene separators delivered superior electrochemical performance. This work offers a new pathway to promote the development of the 2D materials-based functional interlayers for high-performance metal-chalcogenides batteries.

4. Experimental Section

Preparation of $\text{Mo}_2\text{Ti}_2\text{C}_3\text{T}_x$: $\text{Mo}_2\text{Ti}_2\text{AlC}_3$ powder (≈ 1 g) was slowly added to 10 mL of 48% HF acid under magnetic stirring to avoid overheating the solution. After 90 h of etching at 55 °C, the etched powder was centrifuged and washed with de-ionized water five to eight times until the pH reached around 6. Then the sediment obtained after centrifugation was added to 10 mL tetrabutylammonium hydroxide (TBAOH) solution (35 wt% in water) and the suspension was kept stirring for 12 h at an atmosphere temperature. After that, the mixture was washed with de-ionized water five to eight times to remove the redundant TBAOH. Then 100 mL of deaerated water was added to the TBA^+ treated $\text{Mo}_2\text{Ti}_2\text{C}_3\text{T}_x$ sediment, and the solution was sonicated for 1 h under the protection of Ar gas. Subsequently, the mixture was centrifuged at 3500 rpm for 25 min, and the supernatant containing the delaminated few-layer $\text{Mo}_2\text{Ti}_2\text{C}_3\text{T}_x$ (0.5 mg mL^{-1})

was kept for further use.^[46,48] A mild wet-etching method with the LiF + HCl as the etchant was employed to prepare large lateral-sized $\text{Ti}_3\text{C}_2\text{T}_x$ (see details in Supporting Information).

Fabrication of GF@Hybrid MXenes ($\text{Ti}_3\text{C}_2\text{T}_x/\text{Mo}_2\text{Ti}_2\text{C}_3\text{T}_x$) Separators: The as-prepared $\text{Mo}_2\text{Ti}_2\text{C}_3\text{T}_x$ MXene and $\text{Ti}_3\text{C}_2\text{T}_x$ MXene (≈ 95 wt%) were mixed with polytetrafluoroethylene (PTFE, ≈ 5 wt%), and then dispersed into propan-2-ol by ultrasonication to achieve a homogenous suspension, respectively. An amount of 2 mL of the mixed suspension with $\text{Ti}_3\text{C}_2\text{T}_x$ (0.025 mg mL^{-1}) was first dropwise cast onto the surface of a GF (Filttech, glass microfiber $0.7 \mu\text{m}$), then another 2 mL of a $\text{Mo}_2\text{Ti}_2\text{C}_3\text{T}_x$ suspension (0.025 mg mL^{-1}) was cast on the top of $\text{Ti}_3\text{C}_2\text{T}_x$ nanosheets to produce hybrid MXenes coated glass fiber separator (GF@Hybrid MXene). A double amount of the $\text{Ti}_3\text{C}_2\text{T}_x$ suspension coated glass fiber (denoted as GF@ $\text{Ti}_3\text{C}_2\text{T}_x$) was fabricated using the same method as the control sample. The modified separators were all dried overnight in an oven at room temperature with a vacuum.

Material Characterization: Transmission electron microscopy (TEM, JEOL JEM-2011), scanning transmission electron microscope (STEM, JEOL F200), and field emission scanning electron microscopy (FESEM, Zeiss Supra 55VP, Germany) were applied to study the microstructure and morphology of as-prepared samples. X-ray powder diffractometer (Bruker D8) was applied to identify the phases of the specimens using Cu K α radiation ($\lambda = 1.5418 \text{ \AA}$). An X-ray photoelectron spectrometer (Thermo Scientific ESCALAB250Xi, UK, with monochromated Al K alpha (1486.68 eV)) was used to characterize the chemical nature of the specimens. A Park X7 atomic force microscopy (AFM) system was applied to investigate the thickness and lateral sizes of as-prepared MXenes. N_2 gas sorption measurement was conducted at 77 K with a Micromeritics 3Flex analyzer. The Brunauer–Emmett–Teller (BET) method was used to calculate the specific surface area, and the Barrett–Joyner–Halenda (BJH) method was used to calculate the pore volume and pore size distribution. The zeta potentials were measured using Zetasizer Nano (ZS90, Malvern Instruments Ltd., Malvern, England). Raman spectra were tested by applying the Renishaw inVia Raman spectrometer system (Gloucestershire, UK) with the Leica DMLB microscope (Wetzlar, Germany) and the Renishaw helium neon laser source with 17 mW at 633 nm. Thermogravimetric analysis (TGA) was processed by applying an SDT-Q600 simultaneous thermal analyzer in a temperature range from atmosphere temperature to 800 °C with a heating rate of $10 \text{ }^\circ\text{C min}^{-1}$ to investigate the sulfur content of the specimens. Ultraviolet-visible (UV–Vis) spectroscopy (Agilent Cary 60, USA) was applied to investigate the adsorption affinities of the specimens for sodium polysulfides. The in situ XRD testing was carried out at the powder diffraction beamline of the Australia Synchrotron with a 0.6887 \AA wavelength (λ).

Electrochemical Measurements: The electrochemical performances of the modified separators were measured in coin cells (CR2032) with porous carbon/sulfur (pC@S) composites as the cathode materials (see more experimental details in Supporting Information), a sodium metal disc as the anode and an electrolyte ($\approx 20 \mu\text{L}$) of 1 M NaClO_4 (sodium perchlorate, Sigma-Aldrich, 99.95%) in EC/PC (ethylene carbonate/propylene carbonate) (v/v = 1 : 1) with 5% FEC (fluoroethylene carbonate) as the additive. The cathode was prepared by casting a uniform slurry consisting of 80% pC@S, 10% carbon black and 10% PVDF (polyvinylidene fluoride) in NMP (N-methylpyrrolidone) onto the carbon-coated aluminum foil ($\Phi 12 \text{ mm}$), followed by drying in an oven with a vacuum at 80 °C for 12 h. The typical sulfur loading of the cathode is around 1.0 mg cm^{-2} . Afterwards, the battery assembly was assembled in an Ar-filled glovebox ($\text{O}_2 < 0.1 \text{ ppm}$, $\text{H}_2\text{O} < 0.1 \text{ ppm}$). The galvanostatic charge–discharge performances of the batteries were tested by using a LAND CT2001A system in the 0.8–2.8 V voltage range, and the specific capacity was calculated based on the sulfur mass. The electrochemical impedance spectroscopy (EIS) and cyclic voltammograms (CV) investigations were conducted by using a VMP3 multichannel workstation.

Supporting Information

Supporting Information is available from the Wiley Online Library or from the author.

Acknowledgements

Z.H. and S.W. contributed equally to this work. The authors would like to acknowledge the financial support from the Australian Research Council (ARC) through ARC Discovery projects (DP200101249 and DP210101389), ARC Future Fellowship (FT220100561), and ARC Research Hub for Integrated Energy Storage Solutions (IH180100020). Part of the experiment was carried out at the Powder Diffraction Beamline of the Australia Synchrotron.

Open access publishing facilitated by University of Technology Sydney, as part of the Wiley - University of Technology Sydney agreement via the Council of Australian University Librarians.

Conflict of Interest

The authors declare no conflict of interest.

Data Availability Statement

The data that support the findings of this study are available from the corresponding author upon reasonable request.

Keywords

functional interlayers, MXenes, RT Na-S batteries, shuttle effects

Received: December 19, 2022

Revised: February 26, 2023

Published online: April 2, 2023

- [1] Y. Wang, D. Zhou, V. Palomares, D. Shanmukaraj, B. Sun, X. Tang, C. Wang, M. Armand, T. Rojo, G. Wang, *Energy Environ. Sci.* **2020**, *13*, 3848.
- [2] B. Sun, P. Xiong, U. Maitra, D. Langsdorf, K. Yan, C. Wang, J. Janek, D. Schröder, G. Wang, *Adv. Mater.* **2020**, *32*, 1903891.
- [3] Y. X. Wang, B. Zhang, W. Lai, Y. Xu, S. L. Chou, H. K. Liu, S. X. Dou, *Adv. Energy Mater.* **2017**, *7*, 1602829.
- [4] L. Wang, T. Wang, L. Peng, Y. Wang, M. Zhang, J. Zhou, M. Chen, J. Cao, H. Fei, X. Duan, J. Zhu, X. Duan, *Natl. Sci. Rev.* **2021**, *9*, nwab050.
- [5] Y.-X. Wang, J. Yang, W. Lai, S.-L. Chou, Q.-F. Gu, H. K. Liu, D. Zhao, S. X. Dou, *J. Am. Chem. Soc.* **2016**, *138*, 16576.
- [6] Q. Guo, S. Li, X. Liu, H. Lu, X. Chang, H. Zhang, X. Zhu, Q. Xia, C. Yan, H. Xia, *Adv. Sci.* **2020**, *7*, 1903246.
- [7] A. Y. S. Eng, Y. Wang, D.-T. Nguyen, S. Y. Tee, C. Y. J. Lim, X. Y. Tan, M.-F. Ng, J. Xu, Z. W. Seh, *Nano Lett.* **2021**, *21*, 5401.
- [8] Z. Qiang, Y.-M. Chen, Y. Xia, W. Liang, Y. Zhu, B. D. Vogt, *Nano Energy* **2017**, *32*, 59.
- [9] F. Xiao, X. Yang, H. Wang, J. Xu, Y. Liu, D. Y. W. Yu, A. L. Rogach, *Adv. Energy Mater.* **2020**, *10*, 2000931.
- [10] Q. Guo, S. Sun, K.-i. Kim, H. Zhang, X. Liu, C. Yan, H. Xia, *Carbon Energy* **2021**, *3*, 440.
- [11] X. Xu, D. Zhou, X. Qin, K. Lin, F. Kang, B. Li, D. Shanmukaraj, T. Rojo, M. Armand, G. Wang, *Nat. Commun.* **2018**, *9*, 3870.
- [12] X.-m. Zhao, Q. Zhu, S.-d. Xu, L. Chen, Z.-j. Zuo, X.-m. Wang, S.-b. Liu, D. Zhang, *J. Electroanal. Chem.* **2019**, *832*, 392.
- [13] H. Zhang, T. Diemant, B. Qin, H. Li, R. J. Behm, S. Passerini, *Energies* **2020**, *13*, 836.
- [14] H. Liu, W.-H. Lai, Q. Yang, Y. Lei, C. Wu, N. Wang, Y.-X. Wang, S.-L. Chou, H. K. Liu, S. X. Dou, *Nanomicro Lett.* **2021**, *13*, 121.
- [15] L. Medenbach, P. Hartmann, J. Janek, T. Stettner, A. Balducci, C. Dirksen, M. Schulz, M. Stelter, P. Adelhelm, *Energy Technol.* **2020**, *8*, 1901200.
- [16] L. Durai, A. Gopalakrishnan, S. Badhulika, *Mater. Chem. Front.* **2022**, *6*, 2913.
- [17] I. Bauer, M. Kohl, H. Althues, S. Kaskel, *Chem. Commun.* **2014**, *50*, 3208.
- [18] X. Yu, A. Manthiram, *Adv. Energy Mater.* **2015**, *5*, 1500350.
- [19] X. Yu, A. Manthiram, *Chem. Mater.* **2016**, *28*, 896.
- [20] D. Zhou, X. Tang, X. Guo, P. Li, D. Shanmukaraj, H. Liu, X. Gao, Y. Wang, T. Rojo, M. Armand, *Angew. Chem., Int. Ed.* **2020**, *59*, 16725.
- [21] Q. Yang, T. Yang, W. Gao, Y. Qi, B. Guo, W. Zhong, J. Jiang, M. Xu, *Inorg. Chem. Front.* **2020**, *7*, 4396.
- [22] R. Fang, S. Zhao, Z. Sun, D.-W. Wang, R. Amal, S. Wang, H.-M. Cheng, F. Li, *Energy Storage Mater.* **2018**, *10*, 56.
- [23] Q. Zhu, H.-F. Xu, K. Shen, Y.-Z. Zhang, B. Li, S.-B. Yang, *Rare Met.* **2022**, *41*, 311.
- [24] H. Wang, C. Deng, X. Li, D. Yan, M. Xie, S. Zhang, B. Huang, *Chem. Eng. J.* **2021**, *420*, 129681.
- [25] H. Lu, Q. Guo, Q. Fan, L. Xue, X. Lu, F. Zan, H. Xia, *J. Alloys Compd.* **2021**, *870*, 159341.
- [26] T. Yang, B. Guo, W. Du, M. K. Aslam, M. Tao, W. Zhong, Y. Chen, S. J. Bao, X. Zhang, M. Xu, *Adv. Sci.* **2019**, *6*, 1901557.
- [27] H. Al Salem, G. Babu, C. V. Rao, L. M. R. Arava, *J. Am. Chem. Soc.* **2015**, *137*, 11542.
- [28] Z. Cheng, H. Pan, J. Chen, X. Meng, R. Wang, *Adv. Energy Mater.* **2019**, *9*, 1901609.
- [29] X. Zuo, M. Zhen, C. Wang, *Nano Res.* **2019**, *12*, 829.
- [30] R. Sha, P. C. Maity, U. Rajaji, T.-Y. Liu, T. K. Bhattacharyya, *J. Electrochem. Soc.* **2022**, *169*, 013503.
- [31] R. Sha, S. Badhulika, *Electrochim. Acta* **2017**, *251*, 505.
- [32] R. I. Eglitis, G. Borstel, *Phys. Status Solidi A* **2005**, *202*, R13.
- [33] R. Eglitis, *Phys. Scr.* **2015**, *90*, 094012.
- [34] Y. Dong, S. Zheng, J. Qin, X. Zhao, H. Shi, X. Wang, J. Chen, Z.-S. Wu, *ACS Nano* **2018**, *12*, 2381.
- [35] L. Yin, G. Xu, P. Nie, H. Dou, X. Zhang, *Chem. Eng. J.* **2018**, *352*, 695.
- [36] D. Guo, F. Ming, H. Su, Y. Wu, W. Wahyudi, M. Li, M. N. Hedhili, G. Sheng, L.-J. Li, H. N. Alshareef, Y. Li, Z. Lai, *Nano Energy* **2019**, *61*, 478.
- [37] J. Wang, P. Zhai, T. Zhao, M. Li, Z. Yang, H. Zhang, J. Huang, *Electrochim. Acta* **2019**, *320*, 134558.
- [38] N. Li, Y. Xie, S. Peng, X. Xiong, K. Han, *J. Energy Chem.* **2020**, *42*, 116.
- [39] F. Zhang, X. Guo, P. Xiong, J. Zhang, J. Song, K. Yan, X. Gao, H. Liu, G. Wang, *Adv. Energy Mater.* **2020**, *10*, 2000446.
- [40] C. Wang, K. Wu, J. Cui, X. Fang, J. Li, N. Zheng, *Small* **2022**, *18*, 2106983.
- [41] Z. Wang, H. Kim, H. N. Alshareef, *Adv. Mater.* **2018**, *30*, 1706656.
- [42] C. Zhang, B. Anasori, A. Seral-Ascaso, S.-H. Park, N. McEvoy, A. Shmeliov, G. S. Duesberg, J. N. Coleman, Y. Gogotsi, V. Nicolosi, *Adv. Mater.* **2017**, *29*, 1702678.
- [43] M. Ghidui, M. R. Lukatskaya, M.-Q. Zhao, Y. Gogotsi, M. W. Barsoum, *Nature* **2014**, *516*, 78.
- [44] M.-Q. Zhao, X. Xie, C. E. Ren, T. Makaryan, B. Anasori, G. Wang, Y. Gogotsi, *Adv. Mater.* **2017**, *29*, 1702410.
- [45] F. Ming, H. Liang, G. Huang, Z. Bayhan, H. N. Alshareef, *Adv. Mater.* **2021**, *33*, 2004039.
- [46] B. Anasori, Y. Xie, M. Beidaghi, J. Lu, B. C. Hosler, L. Hultman, P. R. C. Kent, Y. Gogotsi, M. W. Barsoum, *ACS Nano* **2015**, *9*, 9507.
- [47] C. Ye, H. Jin, J. Shan, Y. Jiao, H. Li, Q. Gu, K. Davey, H. Wang, S. Z. Qiao, *Nat. Commun.* **2021**, *12*, 7195.
- [48] B. Anasori, C. Shi, E. J. Moon, Y. Xie, C. A. Voigt, P. R. C. Kent, S. J. May, S. J. L. Billinge, M. W. Barsoum, Y. Gogotsi, *Nanoscale Horiz.* **2016**, *1*, 227.
- [49] X. Guo, X. Xie, S. Choi, Y. Zhao, H. Liu, C. Wang, S. Chang, G. Wang, *J. Mater. Chem. A* **2017**, *5*, 12445.
- [50] X. Guo, W. Zhang, J. Zhang, D. Zhou, X. Tang, X. Xu, B. Li, H. Liu, G. Wang, *ACS Nano* **2020**, *14*, 3651.

- [51] C. C. Lai, R. Meshkian, M. Dahlqvist, J. Lu, L. Å. Näslund, O. Rivin, E. N. Caspi, O. Ozeri, L. Hultman, P. Eklund, M. W. Barsoum, J. Rosen, *Acta Mater.* **2015**, *99*, 157.
- [52] L. Óvári, J. Kiss, A. P. Farkas, F. Solymosi, *J. Phys. Chem. B* **2005**, *109*, 4638.
- [53] V. Schier, H. J. Michel, J. Halbritter, *Fresenius J Anal Chem* **1993**, *346*, 227.
- [54] S. Myhra, J. A. A. Crossley, M. W. Barsoum, *J. Phys. Chem. Solids* **2001**, *62*, 811.
- [55] W. Hong, B. C. Wyatt, S. K. Nemani, B. Anasori, *MRS Bull.* **2020**, *45*, 850.
- [56] X. Tang, X. Guo, W. Wu, G. Wang, *Adv. Energy Mater.* **2018**, *8*, 1801897.
- [57] J. Nan, X. Guo, J. Xiao, X. Li, W. Chen, W. Wu, H. Liu, Y. Wang, M. Wu, G. Wang, *Small* **2021**, *17*, 1902085.
- [58] M. S. Nahian, R. Jayan, T. Kaewmaraya, T. Hussain, M. M. Islam, *ACS Appl. Mater. Interfaces* **2022**, *14*, 10298.
- [59] Y. Bai, S. Bi, W. Wang, N. Ding, Y. Lu, M. Jiang, C. Ding, W. Zhao, N. Liu, J. Bian, S. Liu, Q. Zhao, *Soft Mater.* **2022**, *20*, 444.
- [60] M. Hu, Z. Li, T. Hu, S. Zhu, C. Zhang, X. Wang, *ACS Nano* **2016**, *10*, 11344.
- [61] X. Tang, H. Liu, X. Guo, S. Wang, W. Wu, A. K. Mondal, C. Wang, G. Wang, *Mater. Chem. Front.* **2018**, *2*, 1811.
- [62] H. Kim, B. Anasori, Y. Gogotsi, H. N. Alshareef, *Chem. Mater.* **2017**, *29*, 6472.
- [63] Z. Yan, Y. Liang, W. Hua, X.-G. Zhang, W. Lai, Z. Hu, W. Wang, J. Peng, S. Indris, Y. Wang, S.-L. Chou, H. Liu, S.-X. Dou, *ACS Nano* **2020**, *14*, 10284.
- [64] Y. Wang, Y. Lai, J. Chu, Z. Yan, Y. X. Wang, S. L. Chou, H. K. Liu, S. X. Dou, X. Ai, H. Yang, *Adv. Mater.* **2021**, *33*, 2100229.
- [65] C. Ye, Y. Jiao, D. Chao, T. Ling, J. Shan, B. Zhang, Q. Gu, K. Davey, H. Wang, S. Z. Qiao, *Adv. Mater.* **2020**, *32*, 1907557.
- [66] Q. Lu, X. Wang, J. Cao, C. Chen, K. Chen, Z. Zhao, Z. Niu, J. Chen, *Energy Storage Mater.* **2017**, *8*, 77.
- [67] H. Liu, W. Pei, W.-H. Lai, Z. Yan, H. Yang, Y. Lei, Y.-X. Wang, Q. Gu, S. Zhou, S. Chou, H. K. Liu, S. X. Dou, *ACS Nano* **2020**, *14*, 7259.
- [68] H. Yang, S. Zhou, B.-W. Zhang, S.-Q. Chu, H. Guo, Q.-F. Gu, H. Liu, Y. Lei, K. Konstantinov, Y.-X. Wang, S.-L. Chou, H.-K. Liu, S.-X. Dou, *Adv. Funct. Mater.* **2021**, *31*, 2102280.
- [69] B. Sun, P. Li, J. Zhang, D. Wang, P. Munroe, C. Wang, P. H. Notten, G. Wang, *Adv. Mater.* **2018**, *30*, 1801334.
- [70] Z. Hou, Y. Gao, H. Tan, B. Zhang, *Nat. Commun.* **2021**, *12*, 3083.
- [71] J. Qin, H. Shi, K. Huang, P. Lu, P. Wen, F. Xing, B. Yang, M. Ye, Y. Yu, Z.-S. Wu, *Nat. Commun.* **2021**, *12*, 5786.
- [72] H. Wang, W. Bai, H. Wang, D. Kong, T. Xu, Z. Zhang, J. Zang, X. Wang, S. Zhang, Y. Tian, X. Li, C.-S. Lee, Y. Wang, *Energy Storage Mater.* **2023**, *55*, 631.
- [73] R. Amin, M. A. Hossain, Y. Zakaria, *ACS Appl. Mater. Interfaces* **2018**, *10*, 13509.
- [74] G. Deokar, D. Vignaud, R. Arenal, P. Louette, J.-F. Colomer, *Nanotechnology* **2016**, *27*, 075604.
- [75] D. Escalera-López, Y. Niu, S. J. Park, M. Isaacs, K. Wilson, R. E. Palmer, N. V. Rees, *Appl. Catal. B* **2018**, *235*, 84.